JOURNAL OF AIRCRAFT
Vol. 44, No. 4, July–August 2007

Flowfield of a Rotating-Wing Micro Air Vehicle

Manikandan Ramasamy,* Timothy E. Lee,† and J. Gordon Leishman‡
University of Maryland, College Park, Maryland 20742

DOI: 10.2514/1.26415

Experiments were conducted to measure the performance of a rotor, typical of that used on a rotating-wing micro air vehicle, which was shown to develop relatively low hovering efficiency. This inefficiency can be traced to high profile drag losses on the blades and also to the relatively large turbulent and rotational aerodynamic losses that are associated with the structure of the rotor wake. High-resolution flow visualization images have divulged several interesting flow features that appear unique to rotors operating at low Reynolds numbers. The wake sheets trailing from the rotor blades were found to be much thicker and also more turbulent than their higher chord Reynolds number counterparts. Similarly, the viscous core sizes of the tip vortices were relatively large as a fraction of blade chord. However, the flows in the tip vortices themselves were found to be similar, with laminar flow near their core axis and an outer turbulent region. Particle image velocimetry measurements were made to quantify the structure and strength of the wake flow, including the tip vortices. An analysis of the vortex aging process was conducted. A new nondimensional equivalent time scaling parameter is proposed to normalize the rate of growth of the vortex cores that are generated at substantially different vortex Reynolds numbers.

Nomenclature

A	=	rotor disk area, $=\pi R^2$, m^2
A_e	=	effective disk area, m^2
C_d	=	drag coefficient
$\bar{C}_d$	=	average drag coefficient
C_l	=	lift coefficient
C_P	=	rotor power coefficient, $=P/\rho A\Omega^3 R^3$
C_T	=	rotor thrust coefficient, $=T/\rho A\Omega^2 R^2$
c	=	blade chord, m
DL	=	disk loading $=T/A$ or T/A_e, N $\cdot$ m^{-2}
FM	=	figure of merit
P	=	rotor power, N $\cdot$ m s^{-1}
PL	=	power loading, $=T/P$, lb $\cdot$ hp^{-1}
R	=	radius of the blade, m
Re_v	=	vortex Reynolds number, $=\Gamma_v/\nu$
r,θ, z	=	vortex coordinates, m
$\bar{r}$	=	nondimensional radial distance, $=r/r_c$
r_c	=	core radius of the tip vortex, m
T	=	rotor thrust, N
T_e	=	equivalent time, s
t	=	time, s
V_θ	=	swirl velocity, m $\cdot$ s^{-1}
v_h	=	hover induced velocity, m $\cdot$ s^{-1}
W	=	vehicle weight, N
x, y, z	=	DPIV coordinates, m
α	=	Lamb's constant, $=1.25643$
Γ	=	circulation, $=2\pi r V_\theta$, m$^2 \cdot$ s^{-1}
Γ_b	=	bound circulation, m$^2 \cdot$ s^{-1}
Γ_c	=	circulation at the core radius, m$^2 \cdot$ s^{-1}
Γ_v	=	circulation at large distances, m$^2 \cdot$ s^{-1}
δ	=	ratio of apparent to actual viscosity
ζ	=	wake age, deg
κ	=	induced power factor
ν	=	kinematic viscosity, m$^2 \cdot$ s^{-1}
ν_T	=	total kinematic viscosity, $=\nu + \nu_t$, m$^2 \cdot$ s^{-1}
ν_t	=	eddy or tubulent viscosity, m$^2 \cdot$ s^{-1}
ρ	=	air density, kg $\cdot$ m^{-3}
σ	=	rotor solidity
ψ	=	azimuthal position of blade, rad
Ω	=	rotational speed of the rotor, rad $\cdot$ s^{-1}

Received 9 July 2006; revision received 22 March 2007; accepted for publication 23 March 2007. Copyright © 2007 by M. Ramasamy, T. E. Lee, and J. G. Leishman. Published by the American Institute of Aeronautics and Astronautics, Inc., with permission. Copies of this paper may be made for personal or internal use, on condition that the copier pay the $10.00 per-copy fee to the Copyright Clearance Center, Inc., 222 Rosewood Drive, Danvers, MA 01923; include the code 0021-8669/07 $10.00 in correspondence with the CCC.

*Assistant Research Scientist; mani@umd.edu. Member AIAA.
†Minta Martin Intern; telee@umd.edu. Student Member AIAA.
‡Minta Martin Professor of Engineering; leishman@umd.edu. Associate Fellow AIAA.

Introduction

AERODYNAMIC research on hover-capable micro air vehicles (MAVs) has been gaining significant interest from the research community over the past few years. This is because MAVs have potential advantages for performing critical military operations at low risk, such as surveillance, various covert operations, or remote sensing in hazardous environments when airborne chemicals or biological agents exist. Although various definitions of MAVs have been put forth, generally speaking they are defined as flight vehicles that have a maximum dimension that does not exceed 15 cm (6 in.).

Biomimetic (insect-inspired) flapping wings and rotating wings (i.e., rotors) are two different concepts being considered for hovering types of MAVs. Both mechanisms seem to have their own relative advantages and disadvantages. Flapping-wing mechanisms are known to have relatively poor mechanical efficiency, but there have been several hypotheses forwarded [1–4] that claim that flapping-wing concepts can offer better aerodynamic efficiency compared to rotating wings when operated at extremely low chord Reynolds numbers, say below 50,000. Yet, with the generation of turbulent, separated flows with significant vortical flow zones, it is difficult to see how flapping wings can be considered aerodynamically "efficient." Several attempts have been made through computational fluid dynamic simulations, as well as experiments, to prove these hypotheses and to understand the basic physics of flapping-wing flight [5–13]. This work, however, has resulted in mixed levels of success. Computationally, one difficulty is tracking wake vorticity to long times. Experimentally, there are difficulties in measuring accurately the low thrust generated and the corresponding small power required. In both cases, the difficulties of both measuring and predicting the complex three-dimensional, highly unsteady, viscous dominated vortical flows that are present in these types of flowfields cannot be underestimated.

As a result, a comprehensive knowledge of flapping-wing flight has not yet been established to fully explain the aerodynamic performance of insects, or to conclusively prove any of the postulated relative aerodynamic efficiency of flapping-wing based MAVs over rotating-wing concepts. Initial work on the flow diagnostics of a flapping-wing concept is reported in [13], and the focus of the parallel work reported here is on a rotating-wing concept. The primary objective of the work was to examine the wake from a MAV-size, microrotor, and to perform a baseline experiment that helps further the understanding of rotor behavior at low blade Reynolds numbers. The experiment was performed in two stages. First, the performance of the microrotor was measured at various rotational speeds and blade pitch angles. This was followed by flow visualization and digital particle image velocimetry (DPIV) measurements. The work reported in this paper mostly describes the various aerodynamic structures that are present in the flowfield, and those which contribute to determining the net aerodynamic performance of the rotor.

Background

The efficiency of any hovering vehicle can be quantified in terms of an effective power loading, which is defined as the ratio of the vehicle weight (or thrust produced) to the power required to hover, that is, $W/P = T/P = PL$. The induced (ideal) power required to hover is given by $P = T v_h$, where v_h is the minimum average induced velocity through the plane of the rotor disk (or normal to the effective stroke plane of wing flapping [1]) to produce the thrust T. This means that the ideal power loading will be inversely proportional to the induced velocity; this is a fundamental result that comes about based on a solution to the elementary momentum theory [14], which invokes the principles of conservation of mass, momentum, and energy in the flow through the rotor.

Using the momentum theory, the average ideal (minimum) induced velocity can be written in terms of the effective disk loading as

$$v_h = \sqrt{\frac{T}{2\rho A_e}} = \sqrt{\frac{DL}{2\rho}} = \frac{P}{T} = (PL)^{-1} \tag{1}$$

where DL is the effective disk loading, T/A_e. For a rotor $A_e = A$ (rotor disk area), and for a flapping wing the effective disk area A_e is usually based on the net swept area in the stroke plane over one complete wing stroke [1]. The power loading can also be written in terms of the figure of merit FM (i.e., the aerodynamic efficiency) of the system as

$$PL = \frac{T}{P} = \frac{\sqrt{2\rho}FM}{\sqrt{DL}} \tag{2}$$

where the FM accounts for all sources of nonideal losses, that is, other than the induced losses from changes in vertical momentum of the flow. This means that the best hovering efficiency (i.e., the maximum power loading) is obtained when the effective disk loading is minimized and the FM is maximized at that disk loading.

According to the results in Fig. 1, the power loading for hovering flight increases quickly with decreasing effective disk loading (note the logarithmic scales). The best theoretical hovering performance under the stated assumptions is given by the $FM = 1$ line. It will be apparent that hovering concepts that have low effective disk loadings

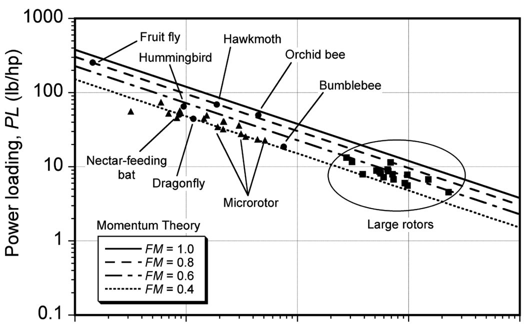

Fig. 1 Power loading versus effective disk loading for biological and mechanical systems. Low effective disk loading always leads to higher hovering efficiency (high power loading).

will always require relatively low power per unit of thrust produced (i.e., they will have higher ideal power loading) and will require less power (and consume less energy) to generate any given amount of thrust.

Therefore, a prerequisite to high hovering efficiency for any type of MAV concept (rotating wing or flapping wing) is always to have a low effective disk loading, although the concept must also have good aerodynamic efficiency (i.e., a high FM). Notice that insects and hummingbirds generally have very low effective disk loadings even though their effective FM values may not necessarily be that high. Measurements made on rotating wings at low disk loadings show efficiency levels comparable to those reportedly achieved by insects.

Because of the relatively low mechanical efficiency of existing flapping-wing MAV concepts, a proven concept such as rotating wing may be the best short-term solution toward successfully developing a hovering-efficient MAV, but only if the rotor can be designed to have both low disk loading and good aerodynamic efficiency. Although good aerodynamic efficiency requires the design of blade airfoil sections with low drag and high lift-to-drag ratios, a major source of performance loss for a hovering rotor is contained within the structure of its blade wake, that is, the induced, rotational, and turbulent losses. It is these losses that will prove difficult to minimize in the quest for more efficient microrotors.

Comprehensive rotor wake measurements have been carried out to help understand the source of wake losses using various scales of rotors, from laboratory model scale to full scale [15–22]. However, no detailed wake measurements have yet been performed on MAV-scale rotors, where the blade tip chord Reynolds numbers lie in the range of 10,000–50,000. This lack of data is not only because of the experimental complexities associated with measuring rotor flows at any scale, but also from the specific measurement challenges that are unique at the MAV-scale level. This includes, but is not limited to, the physical size of the flow structures that are present, which are often too small to be sufficiently resolved with most types of flow diagnostic methods.

The substantial difference in the operating chord Reynolds numbers between a MAV-size rotor and even moderately larger-scale rotors immediately raises several scaling issues that need to be addressed. Clearly, viscous forces are more important for determining the characteristics of the flowfield at these low operating Reynolds numbers. Also, existing experimental evidence suggests that the hovering efficiencies of MAV-scale rotors are substantially lower (with FM values of approximately 0.5) when compared with their high Reynolds number counterparts that have FM values of 0.75 or more [14,23–25]. This suggests that the design goal of improving aerodynamic efficiencies to levels comparable to full-size rotors stems, in part, from an understanding and the minimization by better design of the various sources of losses inside the rotor wake. This includes the wake sheets trailed from each blade, as well as the blade tip vortices and their evolution at low vortex Reynolds numbers.

Experiment

Rotor Performance Measurements

The blades for the microrotor were made of composite carbon fiber and had circular arc, cambered airfoil sections. The top and bottom surfaces of the blades were aerodynamically smooth. The leading and trailing edges of the blades were machined to have rounded edges with circular profiles. The radius of the blade was 86 mm, with a uniform chord of 19 mm, giving a blade aspect ratio of 3.7. The blades had no twist or taper. The rotor had a solidity σ of 0.14 with two blades attached.

The rotor was mounted in a test fixture with one load cell to measure thrust, and another load cell to measure torque. The performance of the rotor was measured at different combinations of rotational speeds and blade pitch angles. Tares were measured and subtracted at different rotational speeds with the blades detached from the hub.

A representative figure of merit plot versus blade loading coefficient is shown in Fig. 2. For reference purposes, two FM curves

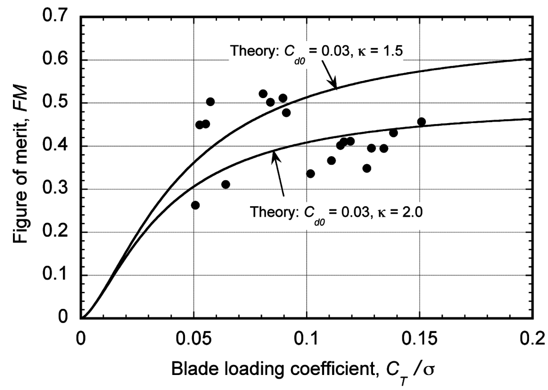

Fig. 2 Figure of merit curve for the microrotor versus blade loading coefficient with momentum theory bounds shown.

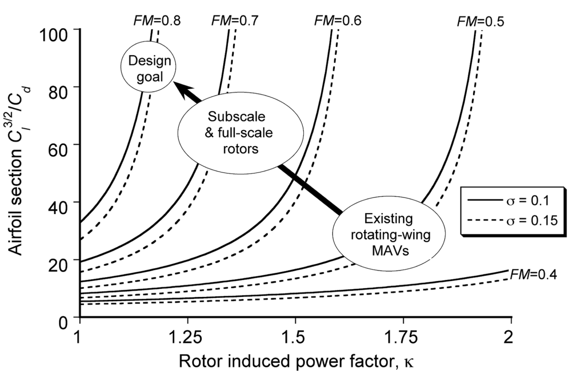

Fig. 3 Rotor figure of merit in terms of wake induced loss and blade section efficiency.

based on simple rotor theory as given by

$$FM = \frac{C_T^{3/2}/\sqrt{2}}{\kappa(C_T^{3/2}/\sqrt{2}) + (\sigma\bar{C}_d/8)} \tag{3}$$

are shown, which are marked here simply to represent bounds rather than the actual predicted performance of the rotor. An average sectional drag coefficient $\bar{C}_d = 0.03$ was assumed, which is typical [23–25] of airfoil section drag coefficients at blade chord Reynolds numbers of 50,000 and also assuming induced power factors κ of 1.5 and 2.0, respectively. Notice that the measurements confirm that the rotor has relatively low aerodynamic efficiency, with an average figure of merit of only about 0.5. Rotor theory gives reasonable bounds on the measurements, and besides indicating significant blade profile losses, also suggests that relatively high induced losses are present compared to those obtained with rotors operating at higher Reynolds numbers (where κ will be less than 1.2).

The problems associated with the design of an efficient rotating-wing MAV now become immediately apparent. By plotting the rotor FM as a function of induced power factor (which is a measure of induced losses) and blade section $C_l^{3/2}/C_d$ (which is a measure of airfoil section efficiency), as shown in Fig. 3, it is apparent that significant reductions in both induced losses and blade section losses are required to improve the FM. Clearly, unless the high induced losses at the MAV scale ($k > 1.5$) can be significantly reduced, no amount of improvement in airfoil section $C_l^{3/2}/C_d$ can lead to increased values of FM. This shows the importance of understanding and minimizing the losses in the rotor wake combined with airfoil section improvements for the best low Reynolds number rotor operation.

Flowfield Measurements

The present experiments included flow visualization and two-component DPIV measurements in the rotor wake. The two-bladed

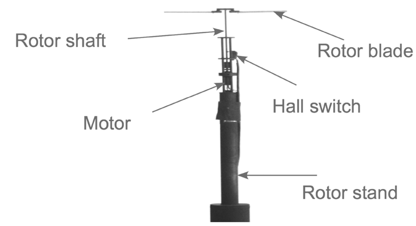

Fig. 4 Photograph of the upper part of the rotor test fixture.

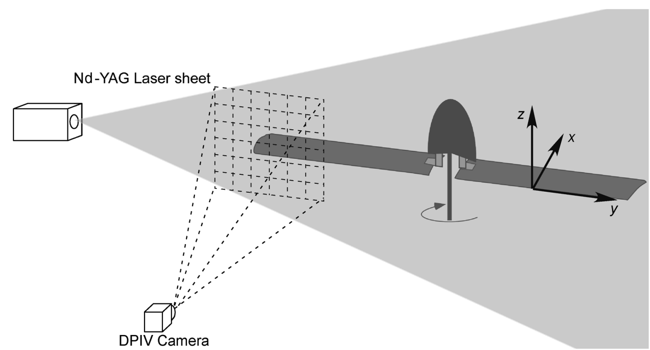

Fig. 5 Schematic showing the DPIV setup.

rotor was placed on a rotor stand, as shown in Fig. 4. For these sets of experiments the rotor was operated at a rotational frequency of 50 Hz with a tip speed of 27.02 ms^{-1}. The operating tip Mach number and Reynolds number based on chord were 0.082 and 34,200, respectively. The measured C_T/σ for the test conditions was 0.0867.

For both the flow visualization and DPIV measurements, the flow at the rotor was seeded with a mineral oil fog. The average sizes of the seed particles were between 0.2 to 0.22 μm in diameter, which was small enough to minimize the particle tracking errors [26]. For the DPIV experiments, the entire test area was uniformly seeded before each sequence of measurements. For the flow visualization, judicious adjustment of the seeder was required to introduce concentrations of fog at the locations needed to clearly identify specific flow structures, such as the tip vortices.

A laser light sheet from a Nd:YAG pulsed laser source capable of frequencies up to 15 Hz was used in synchronization with the rotor frequency to illuminate planes in the flowfield. A fully articulated optical arm was used to locate the light sheet in the required region of focus. A 6.1 megapixel digital still camera was used to acquire all of the images. Digitizing the images relative to a calibration grid provided the required spatial locations of the various observed flow structures, such as the wake sheets and the tip vortices. A schematic of the experimental setup is shown in Fig. 5.

The DPIV system included dual Nd:YAG lasers that were operated in phase synchronization with the rotor, the optical arm to transmit the laser light into the region of interrogation, a digital charge-coupled device (CCD) camera with 1 megapixel resolution placed orthogonally to the laser light sheet, a high-speed digital frame grabber, and DPIV cross-correlation analysis software. The laser could be fired at any blade phase angle around the shaft, enabling DPIV measurements to be made at any required wake age.

The two lasers were fired with a pulse separation time of 15 μs; this corresponded to less than 0.1 deg of blade motion. The interrogation region was focused on a particular region of interest within the image using 50×50 nodes on either side. This covered an interrogation size of 38×44 mm, with 0.75×0.88 mm between adjacent nodes.

DPIV Image Processing

Processing the acquired DPIV images to obtain reliable velocity vectors at this scale was found to be challenging. The biggest advantage of DPIV is its ability to measure the velocity field (over a plane) at a given instant of time rather than the point-by-point measurements typical of laser Doppler velocimetry. However, for a flow that has substantial three-dimensional velocity gradients and/or is combined with large strain or rotational effects (e.g., for vortex flows, as in the present case), the processing of the raw DPIV images needs to satisfy several criteria to result in accurate flowfield measurements [27].

This is further complicated by the aperiodic movement of the tip vortices; this requires individual DPIV images to be spatially orientated so that the centers of the tip vortex in all of the images coincide with each other before the phase averaging. This standard correction for aperiodicity, however, is based on the questionable assumption that the inner region of the vortex flow rotates like a solid body, and so that all of the measurement points inside the vortex are displaced by equal amounts and with the same velocities.

The following describes the procedure used in the present experiment for determining the velocities in the flowfield from the DPIV images. The raw images were first processed using the DPIV cross-correlation analysis software, which yielded the velocity vectors across the entire region of interest. The processing was performed in such a way that the maximum number of interpolated vectors allowed in each image (which has 50×50 nodes) was less than 10. The interrogation window was chosen such that the maximum displacement of the seed particles within the interrogation window was less than one-quarter of the window size. It should be noted that the vortex has nearly zero rotational (swirl) velocity at its center (axis of rotation), and has maximum swirl velocity at its core boundary. The core center, however, has a significant convection velocity. Because the interrogation window size used was uniform in this case (no adaptive grid method has been developed yet) and is optimized for peak velocity measurements, the particle displacement near the vortex center will be a very small fraction of the window size. This may not yield accurate flow velocity results near the vortex core axis.

Furthermore, the combination of centrifugal and Coriollis forces affects the trajectories of the seed particles near the vortex core center [26], which gives a clear seed "void" with a low concentration of seed particles, as can be seen in Fig. 6. This further complicates the problem of making measurements because without enough seed particles, the DPIV analysis may not yield many velocity vectors in those regions. As a result, some of the interpolated vectors obtained during data reduction come from this seed void region.

Accurately measuring the center of the vortex and estimating its core radius are two fundamental requirements for understanding the evolutional properties of tip vortices at any scale. Because the flow velocity vectors are measured through a spatially digitized grid over a given plane in the flowfield, the probability is relatively high that the grid lines will not pass through either the center of the vortex or its core boundary. Identifying the center of the vortex by estimating its centroid of vorticity is a procedure followed by many computational fluid dynamic analysts (e.g., [28]) as well as by some experimentalists (e.g., [17]). However, for the DPIV measurements made in the present study it was found that the grid resolution at this small scale was not completely sufficient to accurately determine the centroid of vorticity by this approach. Therefore, the center of the vortex was defined as the midpoint location of the peak swirl velocity that exists on either side of the vortex flow.

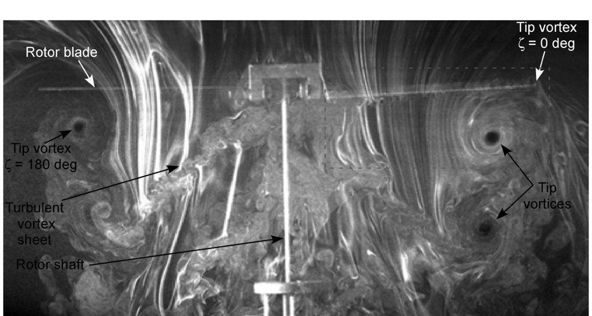

Fig. 6 Flow visualization image acquired at 0 deg wake age showing the trailed blade tip vortices and the inner wake sheet.

This process brings in yet another complication of removing the local convection velocities of the tip vortices through the wake flow. In the present experiment, this was done by choosing an equal number of points on either side of the vortex core and by averaging the tangential component of velocity measured at these points. The velocity components associated with the rotation of the tip vortex were then canceled, leaving only the convection velocity.

The next step was to increase the resolution of the grid to more accurately determine the tip vortex core boundaries. This was done using the Kriging method, which interpolates a value for each output cell by calculating a weighted average of the values at nearby points. The Kriging method analyzes the statistical variation in values over different distances and in different directions to determine the shape and size of the selection area, as well as the set of weighting factors that will produce the minimum error in the interpolated estimate. The grid resolution was then increased by an order that produced a maximum distance of 0.05 mm between adjacent nodes, leaving the maximum possible uncertainty to be less than 0.0125 mm. Once the position of the vortex center was estimated, the procedure was repeated for multiple images that were obtained at the same wake age. Following this, the images were appropriately collocated so that the center of the tip vortices coincided with each other. This allowed for a determination of their phase-averaged flow properties.

Results

Flow Visualization

Flow visualization images were acquired at different wake ages by changing the phase of the blade passage relative to the plane occupied by the laser sheet. Figure 6 shows an example of the concentrated vortices trailing from the tips of blades. Because this was a two-bladed rotor system, every second tip vortex that appears in sequence on the same side of the image is 180 deg of wake age apart.

A closer view of the trailed wake sheet that corresponds to the "boxed" region in Fig. 6 is shown in Fig. 7. The trailed wake sheet can also be seen to roll up into a concentrated vortex near the blade tip. Also, this image reveals the presence of well-organized eddies trailed at regular points along the span of the blades. These eddies identify regions of local concentrated vorticity that result from the merging of boundary layers from the upper and lower surfaces of the blade. In this case, the boundary layers are relatively thick because of the low chord Reynolds numbers ($<50,000$ at the blade tip).

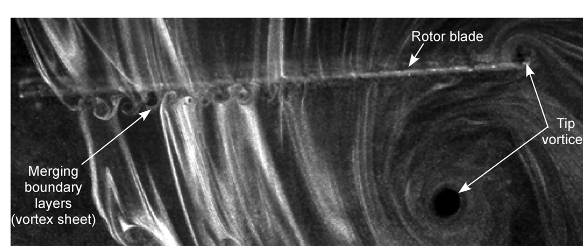

Fig. 7 Closer view of the wake sheets trailing from the rotor blade at 0 deg wake age.

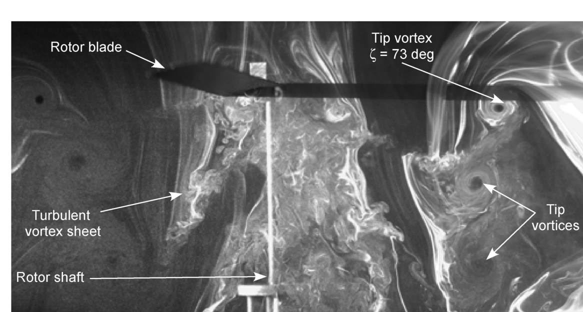

Fig. 8 Flow visualization image obtained at 73 deg of wake age showing the roll up of the vortices at the tip of the blade.

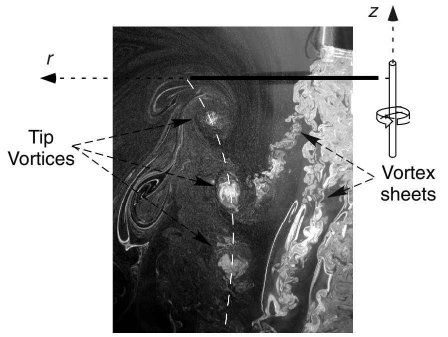

a) Microrotor, Re_v = 35,000

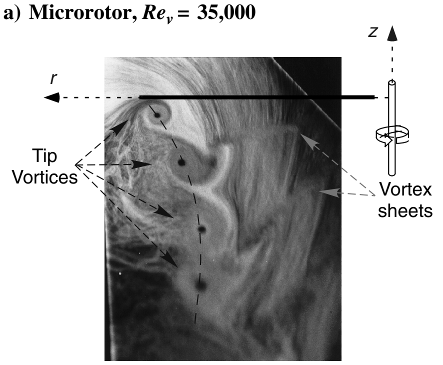

b) Subscale rotor,[14] Re_v = 275,000

Fig. 9 Wake structure behind the blades of rotors operated at two different scales and chord Reynolds numbers.

It can be seen from Fig. 8, that the inboard parts of the helical wake sheets convect axially below the rotor at a much faster rate compared to the tip vortices. This is because they are well inside the slip-stream boundary of the rotor wake, and so the sheets take on increasing inclinations to their initial (almost parallel) orientation to the rotor disk plane. The downstream sheets are much thicker and are also more turbulent than would be obtained with a rotor operating at higher blade Reynolds numbers (see Fig. 9). The net effect is that the helical wake sheets are folded down on top of each other, ultimately occupying a substantial part of the far wake or vena contracta.

Even though the parts of the wake sheets that roll up into the tip vortices appear more turbulent at the MAV scale, the flow near the core axis of the tip vortex is clearly laminar (see Fig. 10). This effect is similar to that found with tip vortices that are trailed from blades operating at higher vortex Reynolds numbers [16]. In this case, a tip vortex generally shows three distinct regions: 1) an inner laminar region where there are no mixing interactions between adjacent layers of fluid, 2) a transitional flow region where there are eddies of several scales, and 3) an outer turbulent region where the flow is mostly turbulent but relatively free of any larger eddies. This multiregion structure arises mainly because of a Richardson number effect [29], which is a rotational stratification effect, and so the relative sizes of the three regions in the vortex flow depend on the vortex Reynolds number Γ_v/ν.

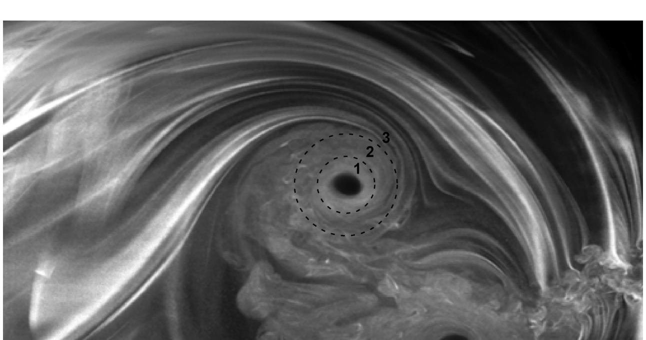

Fig. 10 Flow visualization image obtained at 90 deg of wake age showing the three-region flow structure inside the tip vortices.

DPIV Measurements

Representative DPIV results in the rotor wake that were obtained at 33 deg of wake age are shown in Fig. 11. The resultant velocity vectors $\boldsymbol{V}_\theta + \boldsymbol{V}_r$ show the slip-stream boundary from the rotor. The flow is well organized and has a higher velocity inside the wake slip-stream boundary with an essentially quiescent flow outside this boundary. The mean velocity field shown in this figure was obtained by phase averaging 80 individual DPIV vector fields without correcting for aperiodicity. As previously discussed, it is difficult to apply aperiodicity corrections to larger regions of the flow because the different parts of the wake (at different wake ages) exhibit aperiodic displacements with slightly different magnitudes and frequencies. As a result, correcting the flowfield based on the aperiodic properties at one point in the flow simply introduces a biased and incorrect correction at other locations

The vorticity contours, which are shown in the background of these images, identify the presence of three strong tip vortices. The tip vortex that is closer to the rotor blade (33 deg of wake age) has not yet rolled up completely, resulting in relatively lower levels of vorticity. However, by a wake age of 213 deg, the vortex shows strong vorticity at its core, which then diffuses radially away from the core with further increase in wake age. It is apparent from this image that the tip vortices move radially inward and axially downward from the blade tips as their wake age increases. Also, from the axial location of the vortices below the rotor plane, it can be observed that their axial convection velocity increases after the first blade passage. These are fundamental features common to the wake developments found on rotors at a larger scale [15–17].

Figures 12a and 12b show the average velocity field acquired before and after correcting for the effects of aperiodicity, respectively. On comparing the vorticity contours on the background of both figures, it is apparent that the ensemble phased-averaged vector plot identifies the maximum vorticity at the vortex axis. The results of a simple averaged vector flowfield show the presence of a tip vortex, however, the vorticity is not a maximum at its center. The distribution of vorticity obtained from the corrected flowfield data by making a spanwise cut across the tip vortex is shown in Fig. 13. It can be seen that the maximum value of vorticity is near the vortex axis at all wake ages, as would be expected. Also, it is apparent that the peak value of vorticity reduces (hence diffusing vorticity radially outward) with increasing wake age, again as would be expected based on known tip vortex behavior at higher vortex Reynolds numbers.

The swirl velocity distributions shown in Figs. 14a and 14b were determined by making a cut across the center of the vortex at six

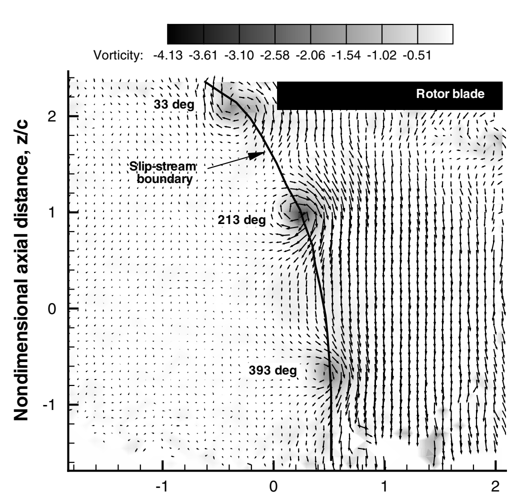

Fig. 11 PIV velocity vector plots obtained at 33 deg of wake age, also showing the slip-stream boundary.

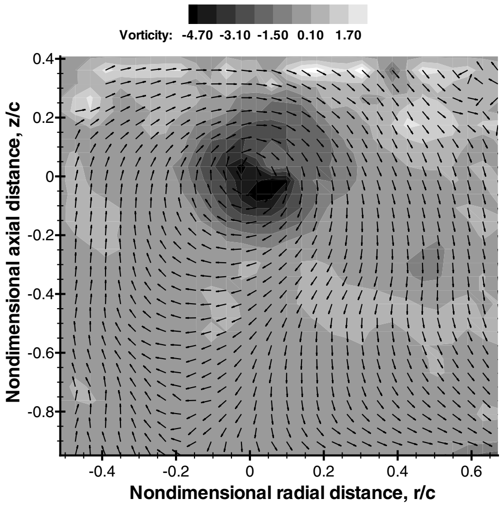

a) Uncorrected

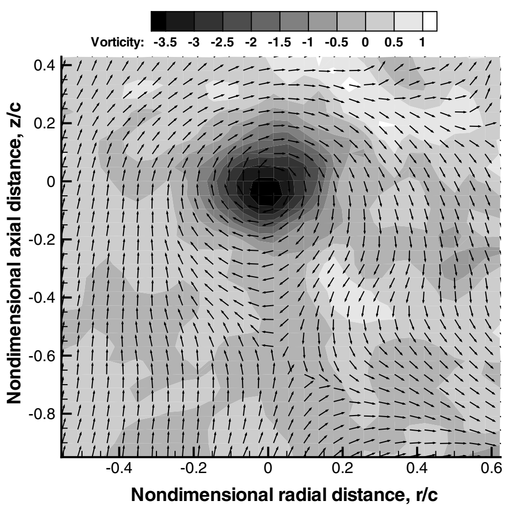

b) Corrected

Fig. 12 PIV velocity vector plots obtained at 26 deg of wake age before and after correcting for the effects of aperiodicity.

different wake ages. The velocity magnitudes were normalized conventionally using the tip speed of the rotor. The classical swirl velocity signature of a tip vortex can be seen in all of the measured velocity profiles. Comparing the swirl velocity profiles measured at 26 and 63 deg of wake age reveals that the peak swirl velocity initially increases with increasing time. Such an observation has been reported earlier with tip vortex measurements obtained from a subscale rotor [30]. However, the initially lower peak swirl velocity in the present case is likely attributed to the increased boundary layer thickness on the blades at this low chord Reynolds number, which could affect the initial development of the tip vortex as it first rolls up behind the blade. This effect can also be seen from Fig. 11, where the tip vortex at a wake age of 213 deg is seen to exhibit higher values of vorticity than at 33 deg. The effects of viscous diffusion can be seen from the swirl velocity profiles at older wake ages, which thereafter exhibit a slow continuous reduction of peak swirl velocity with increasing wake age. This is accompanied by an increase in the vortex core size (defined as the distance between two swirl velocity peaks), which is consistent with conserved core circulation.

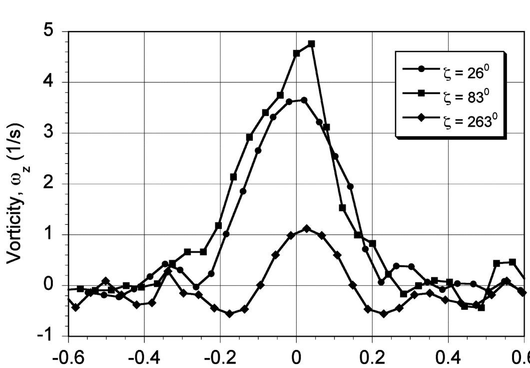

Fig. 13 Streamwise vorticity distribution across the tip vortex for wake ages of 26, 83, and 263 deg.

The circulation distribution in the tip vortices can be determined from the swirl velocity profiles given in Figs. 13 and 14. Based on the assumption that the flow inside the vortex is closely axisymmetric, the circulation distribution can be calculated using the expression

$$\frac{\Gamma}{\Omega R c} = 2\pi\left(\frac{V_\theta}{\Omega R}\right)\left(\frac{r}{c}\right) \tag{4}$$

where r is the radial distance from the center of the tip vortex. The tip vortex strength Γ_v is related to maximum bound circulation on the blade Γ_b and can be estimated from [14] using

$$\frac{\Gamma_v}{\Omega R c} = \frac{\Gamma_b}{\Omega R c} = k\left(\frac{C_T}{\sigma}\right) \tag{5}$$

where $k = 2$ for a rotor blade with ideal twist and $k = 3$ for an untwisted blade [15]. For the current operating condition of this rotor, the estimated value of $\Gamma_b/\Omega Rc$ is 0.256, which is consistent with the measurements of Γ_v. It can be observed from Fig. 15 that the total vortex circulation approaches the value of bound circulation at large radial distances away from the center of the vortex.

Tip Vortex Core Growth

The viscosity of the fluid always plays a substantial role in the evolution of all lift-generated tip vortices. This is especially true in the case of MAV-size rotors, which always create tip vortices that have much lower vortex Reynolds numbers than even moderately larger rotors. The viscous spindown and core growth behavior of these tip vortices are often explained using Lamb-like models. Lamb [31,32] derived an exact solution to the Navier–Stokes (NS) equations to predict the growth rate of laminar vortex cores, where the core radius is given by the simple expression

$$r_c(t) = \sqrt{4\alpha\nu t} \tag{6}$$

where α is Lamb's constant. This result is based on the assumption that the flow inside the vortex is completely laminar, although this cannot be a correct assumption based on the flow visualization results shown previously in Fig. 10. The time t represents the real time elapsed since the vortex was trailed from the blade tip. The use of real time to compare the growth properties of laminar tip vortices at any vortex Reynolds number is entirely appropriate. This is because the transfer of momentum between adjacent layers of fluid is only through molecular diffusion. This implies that the time scale governing core growth is only dependent on the fluid properties (i.e., the kinematic viscosity), which is independent of vortex Reynolds number if the flow is completely laminar.

For real vortices, the transfer of momentum and vorticity between adjacent layers of fluid also occurs because of turbulence. To explain and compare the rate of transfer of radial momentum through the effects of turbulence, the concept of eddy viscosity has been well developed. The modified growth rate of the vortex core to accommodate the effects of turbulence is given by

$$r_c(t, \delta) = \sqrt{r_0^2 + 4\alpha\delta\nu t} \tag{7}$$

where $\delta > 1$ accounts for the increased levels of eddy viscosity in the vortex flow, on average. Here, r_0 prevents the singular solution at time $t = 0$ by having a definite (viscous) core size. It is known that δ is a function of vortex Reynolds number [29,33,34]. An increase in vortex Reynolds number gives an increase in turbulence that, in turn,

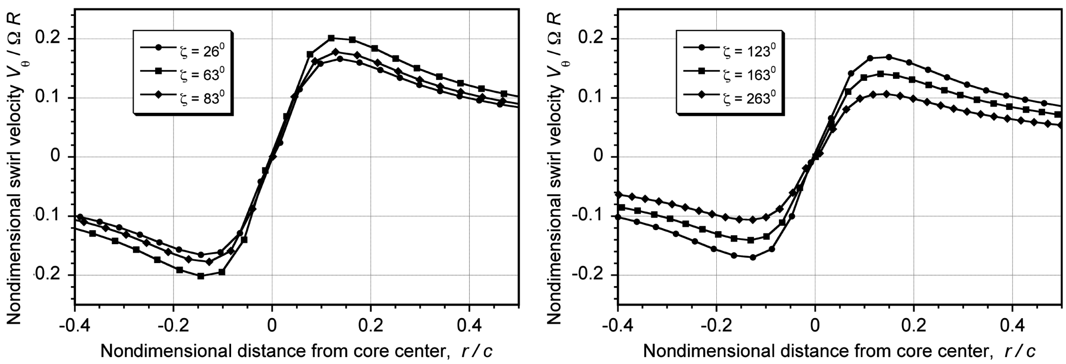

a) Early wake ages b) Older wake ages

Fig. 14 Swirl velocity distributions across the tip vortex at several wake ages.

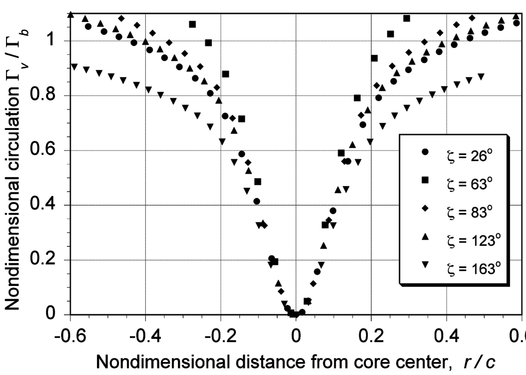

Fig. 15 Measured circulation distribution across the tip vortices at various wake ages.

increases the average eddy viscosity in the vortex flow and so increases the vortex core growth rate.

Vortex models based on the Lamb–Oseen model have been modified empirically to include the effects of turbulence, which then have different values of average eddy viscosity at different vortex Reynolds numbers [29]. This means that the time scale (which is dependent on the total viscosity) will also change for varying values of vortex Reynolds numbers. Therefore, the comparison of vortex core growth measurements acquired at significantly different Reynolds numbers using the same time scale is probably not appropriate, and the time scale must be normalized by an appropriate scaling parameter that must take into account Reynolds number effects.

This concept can be better explained by plotting the measured core size of the tip vortices and comparing them to results measured from a subscale rotor that has generated vortices at higher vortex Reynolds numbers, which is shown in Fig. 16. It can be seen from this figure that the tip vortex core measured from the MAV-size rotor appears much higher when compared at the same wake age. Despite the fact that the vortex Reynolds number of the MAV-size rotor is about 5 times smaller than those even in the subscale measurements, when plotted versus wake age the value of δ appears to be twice that of the subscale measurements. This would imply that the tip vortices from the MAV-size rotor at the same age contain, on average, twice the amount of turbulence compared to the vortices generated by the subscale rotor. This does not seem reasonable bearing in mind the very much lower vortex Reynolds numbers found at the MAV scale.

This problem can be further understood by plotting the tip vortex measurements in terms of equivalent peak swirl velocity and equivalent downstream distance using an Iversen-type correlation curve [34], as shown in Fig. 17. Tip vortex measurements acquired at different vortex Reynolds numbers (from both rotating wings and fixed wings) have been plotted here, along with Iversen's solution. It is apparent from this figure that the measurements made with the microrotor correlate quite well with the Iversen model. This suggests that the growth characteristics of the tip vortices trailed from a microrotor should be substantially similar to that generated by any type of tip vortex. A substantially higher value of δ (growth rate) suggested by Fig. 16, therefore, cannot be physical.

Equivalent Time

The viscous core size and growth rate of the vortex at any given time depend at least on four parameters: 1) the initial core size as it leaves the blade, 2) the total viscosity of the fluid (kinematic plus eddy, $\nu + \nu_t$), 3) time or wake age, and 4) the strain (stretching or squeezing) experienced by the filament as it convects in the flow. The initial core size r_0 takes into account the thickness of the boundary layer on the blade (which also rolls up into the tip vortices) and the

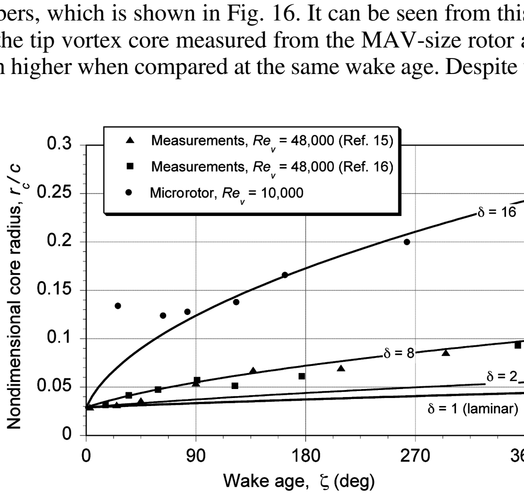

Fig. 16 Comparison of the measurements of tip vortex core size at different Reynolds numbers with increasing wake age.

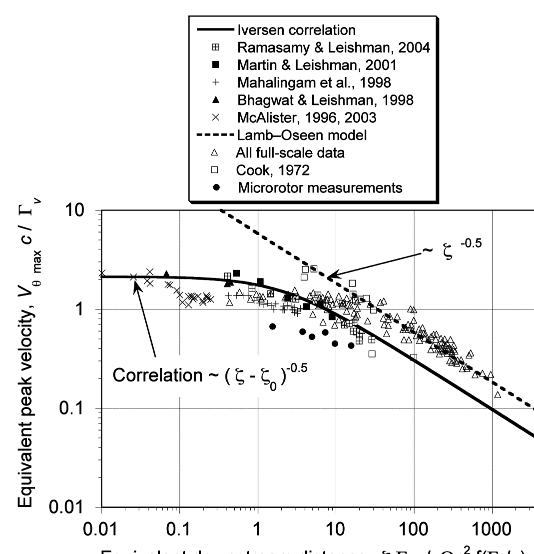

Fig. 17 Iversen type of correlation function used to consolidate all of the tip vortex measurements.

total viscosity addresses the effects of scaling (vortex Reynolds number Γ_v/ν). It can be seen that the tip vortex cores trailed from the microrotor blades show a reduction in size before starting to increase, the latter which is from the effects of viscous and turbulent diffusion. The initial reduction in core size indicates the delayed completion in the roll up of the tip vortices. Positive strain rates, which are known to be substantial during the vortex roll-up process, are known to counter the effects of diffusion to result in a reduced core size [16]. Even though there is a reduction in core size, the absolute size of the vortex core is still relatively larger than is found at higher Reynolds numbers. This is expected and, as mentioned earlier, is likely partly a result of the relatively thick boundary layers on the blade and their influence during the initial roll up of the vortices.

Using dimensional analysis, an equivalent time parameter can be defined as

$$T_e = \frac{t}{c^2/\Gamma_v} = \frac{\zeta/\Omega}{c^2/\Gamma_v} = \frac{\zeta R}{c}\left(\frac{\Gamma_v}{\Omega R c}\right) \tag{8}$$

with the assumption that any strain effects on the vortex flow are negligible. Such an assumption is valid once the roll up of the tip vortices is complete. This equivalent time parameter can also be derived from the nondimensional similarity variable used in the Ramasamy–Leishman vortex model [29], which is an exact solution to the Navier–Stokes equations for a vortex flow. Any analysis made to understand the growth rate of the tip vortex cores that are evolving at different vortex Reynolds numbers should be made using an equivalent time parameter. It can be observed that the equivalent time parameter is a function of the principal permanent characteristic of the tip vortex, namely, the total vortex circulation Γ_v. It should be remembered here that the eddy viscosity, which represents a measure of turbulence, is a function of the circulation contained within the vortex. As a result, by taking into account the total vortex circulation, the equivalent time accounts for the time scales associated with the turbulence intensities within the vortex flow.

Using this equivalent time concept, the measured core growth of the tip vortex is compared in Figs. 18 and 19 with measurements from

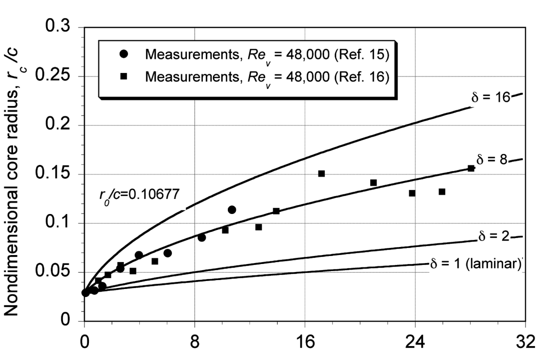

Fig. 18 Variation of the tip vortex core growth versus normalized time.

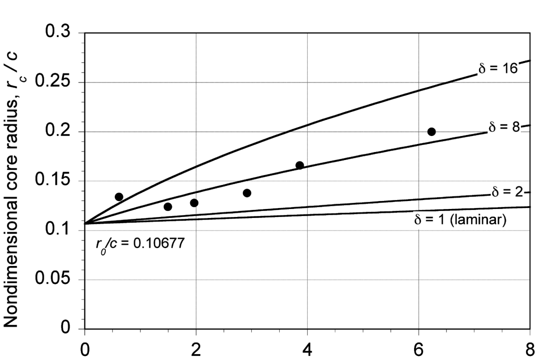

Fig. 19 Variation of the tip vortex core growth with normalized time for the MAV-scale rotor measurements.

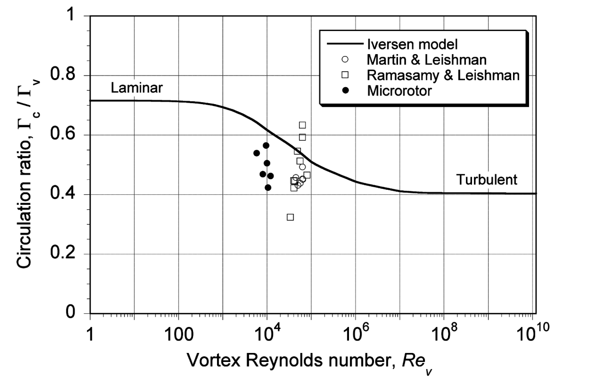

Fig. 20 Normalized circulation of the tip vortices from the MAV-scale rotor relative to Iversen's solution.

the larger subscale rotor. First, by plotting in terms of the equivalent time T_e, the vortex cores trailed from the microrotor blades showed a reduction in growth rate when compared with the previous predictions shown in Fig. 16. Second, when comparing the results in the two figures, it is apparent that when plotted in terms of the equivalent time T_e, the vortex core growth for the MAV-size rotor is nearly identical to that of the subscale rotor. A value of δ equal to 8 seems to represent the growth characteristics of both of the tip vortices, even though they have substantially different Reynolds numbers. However, the core growth is still higher than what is expected based on the operating vortex Reynolds number.

The observed higher growth rate of the tip vortices from the microrotor can be further explained by plotting the ratio of core circulation to the total vortex circulation as a function of vortex Reynolds number (as obtained from the Iversen's exact solution to the NS equations [34]—see the results in Fig. 20). A larger value for this ratio (0.707 for laminar flow) would mean that the vortex will diffuse its contained vorticity more slowly. It is apparent that the value of this ratio is smaller when compared with the Iversen's solution at the measured vortex Reynolds number (10,000). However, this ratio can be seen to be comparable to the measurements from rotors operating at higher vortex Reynolds numbers (50,000). Such a lower value of this ratio would mean that the diffusion of vorticity is faster and may have its source from the observed increase in boundary layer thickness on the blade (because of the lower chord Reynolds number), although further work must be done to examine this particular hypothesis.

Conclusions

The performance of a small rotor, typical of application to a rotating-wing micro air vehicle, has been measured. This was accompanied by flow visualization and DPIV measurements in the rotor wake. It has been shown that the wakes generated by the rotor blades are thicker and more turbulent than compared to the wakes generated by rotors operating at higher chord Reynolds numbers. A closer examination of the wake sheets revealed a very organized series of discrete eddies that were trailed along the blade span. The tip vortex structure also showed some important differences from those expected on rotors operated at larger chord Reynolds numbers. The following specific conclusions have been drawn from this study:

1) The overall hovering performance (power loading) of a MAV will directly depend on its effective disk loading and its aerodynamic efficiency or figure of merit (FM). Decreasing the effective disk loading is a design goal that increases the power loading and attempting to raise the FM by reducing both induced and profile losses are the primary requirements for developing an efficient hovering MAV.

2) The maximum FM values measured were found to be substantially lower (no more than 0.5) than for rotors operated at higher chord Reynolds numbers (which often approach 0.8). The increased boundary layer thicknesses on the blades and the more turbulent wake (both of which increase losses) contribute to the

substantially reduced efficiency of rotating wings that are operated at low chord Reynolds numbers.

3) Viscous effects, which are relatively more important at low Reynolds numbers, appear to affect the initial formation and roll up of the blade tip vortices, which do not reach their full circulation until some distance downstream of the blade. This roll up is followed by the viscous and turbulent diffusion of vorticity, which results in an increased tip vortex core size and a reduced peak swirl velocity with increasing wake age.

4) The properties of blade tip vortices that are measured at different vortex Reynolds numbers must be properly analyzed on the same equivalent time scale. It was shown that by using an equivalent time parameter to compare the vortex core sizes, the growth rate of the tip vortices is similar to that found at higher vortex Reynolds numbers.

Acknowledgments

This research was supported, in part, by the Multi-University Research Initiative under Grant ARMY W911NF0410176. Gary Anderson and Thomas Doligalski were the technical monitors. The authors wish to acknowledge the contributions of Jayant Sirohi and Moble Benedict in helping to measure the performance of the microrotor. The authors also wish to acknowledge Tyler Huismann and Bradley Johnson for their contributions to this work.

References

[1] Willmott, A. P., Ellington, C. P., and Thomas, A. L. R., "Flow Visualization and Unsteady Aerodynamics in the Flight of the Hawkmoth, Manduca Sexta," *Philosophical Transactions of the Royal Society of London, Series B: Biological Sciences*, Vol. 352, No. 1351, March 1997, pp. 303–316.

[2] Srygley, R. B., and Thomas, A. L. R., "Unconventional Lift-Generating Mechanisms in Free-Flying Butterflies," *Nature (London)*, Vol. 420, No. 6916, Dec. 2002, pp. 660–662.

[3] Buckholz, R. H., "Measurements of Unsteady Periodic Forces Generated by the Blowfly Flying in Wind Tunnel," *The Journal of Experimental Biology*, Vol. 90, No. 1, Feb. 1981, pp. 163–173.

[4] Weis-Fogh, T., "Quick Estimates of Flight Fitness in Hovering Animals Including Novel Mechanisms for Lift Production," *The Journal of Experimental Biology*, Vol. 59, No. 1, Aug. 1973, pp. 169–230.

[5] Minotti, F. O., "Unsteady Two-Dimensional Theory of a Flapping Wing," *Physical Review E*, Vol. 66, No. 051907, 2002, pp. 1–10.

[6] Wang, Z. J., "Two-Dimensional Mechanism for Insect Hovering," *Physical Review Letters*, Vol. 85, No. 10, 2000, pp. 2216–2219.

[7] Liu, H., and Kawachi, K., "A Numerical Study of Insect Flight," *Journal of Computational Physics*, Vol. 146, No. 1, 1998, pp. 124–156.

[8] Sun, M., and Tang, J., "Unsteady Aerodynamic Force Generation by a Model Fruit Fly Wing in Flapping Motion," *The Journal of Experimental Biology*, Vol. 205, No. 1, 2002, pp. 55–70.

[9] Birch, J. M., and Dickinson, M. H., "Spanwise Flow and the Attachment of Leading-Edge Vortex on Insect Wings," *Nature (London)*, Vol. 412, No. 6848, 2001, pp. 729–733.

[10] Singh, B., Ramasamy, M., Chopra, I., and Leishman, J. G., "Insect Based Flapping Wings For Micro Hovering Air Vehicles: Experimental Investigations," *American Helicopter Society International Specialists Meeting on Unmanned Rotorcraft, Phoenix, AZ*, 18–20 Jan. 2005.

[11] Ellington, C. P., and Usherwood, J. R., "Lift and Drag Characteristics of Rotary and Flapping Wings," *Fixed and Flapping Wing Aerodynamics for Micro-Air Vehicle Applications*, edited by T. A. Mueller, Vol. 195, AIAA Progress in Aeronautics and Astronautics, AIAA, Reston, VA, 2001, pp. 231–248, Chap. 12.

[12] Tarascio, M., Ramasamy, M., Chopra, I., and Leishman, J. G., "Flow Visualization of MAV Scaled Insect Based Flapping Wings in Hover," *Journal of Aircraft*, Vol. 42, No. 2, March 2005, pp. 355–360.

[13] Ramasamy, M., Leishman, J. G., and Singh, B., "Wake Structure Diagnostics of a Flapping Wing MAV," *2005 SAE Transactions Journal of Aerospace*, Vol. 114, No. 1, Feb. 2006, pp. 907–919.

[14] Leishman, J. G., *Principles of Helicopter Aerodynamics*, 2nd ed., Cambridge Univ. Press, New York, 2006.

[15] Martin, P. B., Pugliese, G., and Leishman, J. G., "High Resolution Trailing Vortex Measurements in the Wake of a Hovering Rotor," *Journal of the American Helicopter Society*, Vol. 49, No. 1, Jan. 2003, pp. 39–52.

[16] Ramasamy, M., and Leishman, J. G., "Interdependence of Diffusion and Straining of Helicopter Blade Tip Vortices," *Journal of Aircraft*, Vol. 41, No. 5, Sept.–Oct. 2004, pp. 1014–1024.

[17] McAlister, K., "Rotor Wake Development During the First Rotor Revolution," *Journal of the American Helicopter Society*, Vol. 49, No. 4, Oct. 2004, pp. 371–390.

[18] Heineck, J. T., Yamauchi, G. K., Wadcock, A. J., and Lourenco, L., "Application of Three-Component PIV to a Hovering Rotor Wake," *American Helicopter Society 56th Annual National Forum, Virginia Beach, VA*, 2–4 May 2000.

[19] Yu., Y. H., and Tung, C., "The HART-II Test: Rotor Wakes and Aeroacoustics with Higher Harmonic Pitch Control (HHC) Inputs," *American Helicopter Society 58th Annual National Forum, Montreal, Canada*, 11–13 June 2002.

[20] Cook, C. V., "The Structure of the Rotor Blade Tip Vortex," Paper 3, Aerodynamics of Rotary Wings, AGARD CP-111, 13–15 Sept. 1972.

[21] Kraft, C. C., "Flight Measurements of the Velocity Distribution and Persistence of the Trailing Vortices of an Airplane," NACA TN 3377, 1955.

[22] Boatwright, D. W., "Three-Dimensional Measurements of the Velocity in the Near Flow Field of a Full-Scale Hovering Rotor," Mississippi State University Report EIRS-ASE-74-4, 1974.

[23] Bohorquez, F., Samuel, P., Sirohi, J., Pines, D., Rudd, L., and Perel, R., "Design Analysis and Hover Performance of a Rotating Wing Micro Air Vehicle," *Journal of the American Helicopter Society*, Vol. 48, No. 2, April 2003, pp. 80–90.

[24] Hein, B., and Chopra, I., "Hover Performance of a Micro Air Vehicle: Rotor at Low Reynolds Number," *American Helicopter Society International Specialists' Meeting on Unmanned Rotorcraft, Phoenix, AZ*, 18–20 Jan. 2005.

[25] Ramasamy, M., Johnson, B., and Leishman, J. G., "Toward Understanding the Aerodynamic Efficiency of a Hovering Micro-Rotor," *American Helicopter Society International Specialists' Meeting on Unmanned Rotorcraft, Phoenix, AZ*, 23–25 Jan. 2007.

[26] Leishman, J. G., "On Seed Particle Dynamics in Tip Vortex Flows," *Journal of Aircraft*, Vol. 33, No. 4, July/Aug. 1996, pp. 823–825.

[27] Ramasamy, M., and Leishman, J. G., "Benchmarking PIV with LDV for Rotor Wake Vortex Flows," AIAA Paper 2006-3479, June 2006, *AIAA Journal* (to be published).

[28] Duraisamy, K., and Baeder, J., "Studies on Tip Vortex Formation, Evolution and Control," Ph.D. Dissertation, University of Maryland, College Park, MD, April 2005.

[29] Ramasamy, M., and Leishman, J. G., "A Generalized Model For Transitional Blade Tip Vortices," *Journal of the American Helicopter Society*, Vol. 51, No. 1, Jan. 2006, pp. 92–103.

[30] Leishman, J. G., Baker, A., and Coyne, A., "Measurements of Rotor Tip Vortices Using Three-Component Laser Doppler Velocimetry," *American Helicopter Society International Aeromechanics Specialists' Conference, Bridgeport, CT*, 11–13 Oct. 1995.

[31] Oseen, C. W., "Uber Wirbelbewegung in Einer Reibenden Flüssigkeit," *Arkiv för Matematik, Astronomi och Fysik.*, Vol. 7, No. 14, 1911, pp. 14–21.

[32] Lamb, H., *Hydrodynamics*, 6th ed., Cambridge Univ. Press, Cambridge, England, U.K., 1932.

[33] Squire, H. B., "The Growth of a Vortex in Turbulent Flow," *Aeronautical Quarterly*, Vol. 16, Aug. 1965, pp. 302–306.

[34] Iversen, J. D., "Correlation of Turbulent Trailing Vortex Decay Data," *Journal of Aircraft*, Vol. 13, No. 5, May 1976, pp. 338–342.